

Temperature and density in a polar plume – measurements from CDS/SOHO

P.R. Young¹, J.A. Klimchuk², and H.E. Mason¹

¹ Department of Applied Mathematics and Theoretical Physics, University of Cambridge, UK

² Naval Research Laboratory, Washington D.C., USA

Received 23 November 1998 / Accepted 14 June 1999

Abstract. A detailed analysis of a particularly intense polar plume observed on the 25th of October, 1996, by the Coronal Diagnostic Spectrometer (CDS) on board the Solar and Heliospheric Observatory (SOHO) is presented. Above the limb, emission measure distributions derived for both the plume and a section of coronal hole background are found to be sharply peaked at approximately 1.0–1.1 million degrees in both regions. The temperature rises with height in the background, but no evidence is found for a rising temperature in the plume. The density of the background is approximately 10^8 electrons/cm³ and falls with height. In the plume the density is between 3.8 and 9.5×10^8 electrons/cm³, and exhibits no decrease with height up to 70 000 km.

The plume base is visible on the solar surface and shows a strong brightening lying directly below the main body of the plume. This brightening has a temperature of 2 000 000 K, and a density of 2.5 – 5.6×10^9 electrons/cm³. Images from lines formed at different temperatures suggest that the morphology of the base is consistent with an emerged bipole in a region of unipolar magnetic flux.

A measurement of the Mg/Ne relative abundance is made at two transition region brightenings at the base of the plume. An enhancement of only 1.5 is found over the photospheric value.

Considerations of the geometry of both the high temperature brightening at the base of the plume and the off-limb section give filling factors of 0.5 and 1.0, respectively.

Key words: Sun: UV radiation – Sun: abundances – Sun: solar wind

1. Introduction

Polar plumes are a common feature of solar coronal holes and they are best seen in white light and EUV images. For a white-light observation, it is necessary to use a coronagraph and the plumes appear as rays (indeed, plumes are often referred to as ‘polar rays’ in the context of white light data). These rays strongly suggested that the material is confined by a global magnetic field which has a near-dipole character. An advantage of the white-light observations is that the plumes can be detected

to quite large distances: $1.5 R_{\odot}$ with ground-based telescopes, $5 R_{\odot}$ with SPARTAN (Fisher & Guhathakurta 1995) and, more recently, up to $15 R_{\odot}$ with the LASCO instrument on SOHO (Sect. 2.4 of DeForest et al. 1997). Shortcomings of EUV instrumentation prevent this in the EUV, but a major advantage is that the bases of the plumes can be identified against the solar disk. This has enabled plumes to be identified with specific magnetic features at the solar surface.

Key developments in the observation and theory of plumes are described in Sect. 2, while the CDS instrument is described in Sect. 3. The rest of this paper discusses the new observations.

2. Previous work on polar plumes

2.1. Observations

White light observations permit measurements of the electron density in plumes, but not the temperature. The density determinations follow through first establishing a density for the background coronal hole and then comparing the white light brightness in the plume with the background, e.g., Sect. 2 of van de Hulst (1950). Uncertainties arise because the line-of-sight thickness and the filling factor of the plume volume must be assumed.

In the EUV one finds emission lines formed from ions present over narrow temperature intervals, and simply the existence of a plume in a given line gives a rough indication of the temperature. A more precise measurement can be obtained through studying the ratio of two lines formed at different temperatures (e.g., Sect. 3 of Ahmad & Withbroe 1977, where the Mg x 625 Å and O vi 1032 Å lines were used). A density estimate can be obtained from the absolute intensity of an emission line, although this requires certain assumptions regarding element abundances, filling factors and the size of the emitting region.

These uncertainties can be avoided by using a *density diagnostic* line pair from a single ion (e.g., Sect. 3.4 of Mason & Monsignori-Fossi 1994), and Widing & Feldman (1992) use the 436.73+436.67/430.47 Mg VIII diagnostic to give a density of 1×10^9 cm⁻³ for an intense plume observed by the Skylab S082A EUV spectrometer. Further, a *filling factor* of 1/3 was also estimated for the plume. By comparing lines of magnesium

Send offprint requests to: P.R. Young (P.R.Young@damtp.cam.ac.uk)

and neon, Widing & Feldman also found the significant result that the Mg/Ne abundance ratio was enhanced over the photospheric value by a factor 10. The Widing & Feldman (1992) analysis is most similar to that presented here from the CDS data. We note that, with the S082A instrument, spectral and spatial dimensions are unavoidably mixed and so it was not possible for Widing & Feldman to subtract the contribution of the coronal hole background from the plume line intensities. In the present case, CDS allows spectral and spatial dimensions to be fully resolved, and it is found that the background forms a substantial contribution to intensities measured from the plume.

The launch of the Solar and Heliospheric Observatory (SOHO) in December 1995 during solar minimum has led to a number of studies of polar plumes and coronal hole regions. Hassler et al. (1997) have used SUMER (Solar Ultraviolet Measurements of Emitted Radiation) observations of the O VI 1032 Å line to show that plume regions are some 10–50% brighter than non-plume regions, but that line widths are around 10–15% narrower. There are several possible reasons for these observations (see Sect. 3 of Hassler et al.), including the plume having a lower temperature than the background. Evidence for this is presented in Wilhelm et al. (1998) who use the temperature sensitive Mg IX 706/750 line ratio to determine the electron temperature in both plume and interplume regions. In the plume, the temperature is found to fall with height, with values of $\approx 750\,000$ K at heights up to $\approx 180\,000$ km, $530\,000$ K at $250\,000$ km, and $330\,000$ K at $420\,000$ km. The electron temperatures in the interplume region lie between $750\,000$ K and $850\,000$ K up to heights of $210\,000$ km.

Another method of determining the electron temperature in off-limb regions is presented in David et al. (1998). Here the strongly temperature sensitive O VI 173 Å/1032 Å ratio is used to yield coronal hole temperatures of $800\,000$ K close to the solar limb, $1\,000\,000$ K at $105\,000$ km, and $400\,000$ K at $210\,000$ km. The data used contain averages over both plume and interplume regions. Note that the 173 Å line was observed with the CDS instrument, while the 1032 Å line was observed with SUMER. The uncertainty in the cross-calibration of the two instruments was eliminated by performing measurements in an off-limb quiet Sun region and normalising the derived temperatures close to the limb to a “standard” value of $\log T = 6.1$.

Abundances in off-limb plume and interplume regions have been studied by Wilhelm & Bodmer (1998) who presented a preliminary study of the Mg/Ne abundance ratio in their SUMER plume observations, and deduce enhancements of 1.7 and 3.5 over photospheric values at heights of $35\,000$ and $70\,000$ km.

A key aim of SOHO was to obtain joint observations of the Sun using both SOHO instruments and ground-based observatories, and preliminary results from one such observing program aimed at polar plumes have been presented in DeForest et al. (1997). The data studied are from 7 and 8 March 1996 and impressive montages of the different instrument images are shown in Figs. 10 and 11 of this work. The MDI instrument took magnetograms in the coronal hole and showed that, although the plume bases are predominantly unipolar, they are considerably

more mixed than other unipolar concentrations in the coronal hole that did not give rise to plumes. Comparisons of the Fe XII and Fe IX/X images from EIT revealed the plumes to be cooler than the interplume regions, while high cadence EIT image sequences showed that the plume intensity varied at the 10–20% level on scales $\lesssim 10$ arc sec, while remaining relatively constant at larger scales. The Normal Incidence Spectrometer (NIS) of CDS was used in *viewfinder mode* (i.e., the large 90×240 slit was used, giving images rather than spectra) for these observations and showed that the plume footpoints coincided with O V brightenings in the network.

2.2. Theory

Plumes are widely believed to be due to the emergence of small bipolar flux regions into coronal holes, with the subsequent reconnection giving rise to EUV enhancements at the plume base and mass input along the open field lines of the plume (see Wang & Sheeley 1995).

Wang (1994) discusses previous theoretical work on polar plumes and also extends this to provide a new model. In this 1D model, magnetic flux tubes extending out into the solar wind are considered. It is found that, in order to predict typical solar wind values of velocity, temperature and mass flux at ~ 1 AU, a ‘global’ heating operating on length scales $H_m \sim 1$ AU is required. However, the pressure at the tube base scales as the inverse of H_m and so the large pressures seen in the bases of plumes cannot be obtained. To resolve this problem, Wang (1994) introduces an additional heating term with a scale height H_b such that $H_b \ll R_\odot$. In this model, the temperature in the plume shows a sharp maximum just above the plume base – the temperature then falling for a short distance before rising as the plume extends out into the solar wind. Without the additional heating term, the temperature simply rises monotonically, attaining a higher asymptotic value than with the base heating term.

Del Zanna et al. (1997) present a 2D model of a plume, axisymmetric about the plume axis, which allows different field lines to have different temperatures. They also consider the effects of adding a bi-polar flux concentration at the plume base, which reproduces the super-radial expansion often observed there.

3. The coronal diagnostic spectrometer

The Coronal Diagnostic Spectrometer (CDS) on board SOHO is described thoroughly in Harrison et al. (1995, 1997) and the main features are noted here. There are two distinct spectrometers: the Grazing Incidence (GIS) and Normal Incidence (NIS). Only data from the NIS are presented here. The NIS obtains both spectral information and one dimension of spatial information simultaneously, with images obtained by rastering in the remaining spatial dimension (usually solar-x). For any one pointing of the instrument a 4×4 arc min² region can be viewed with around 3 arc sec resolution (the resolution of the telescope). Two spectral wavebands are observed simultaneously, 307–379 Å and

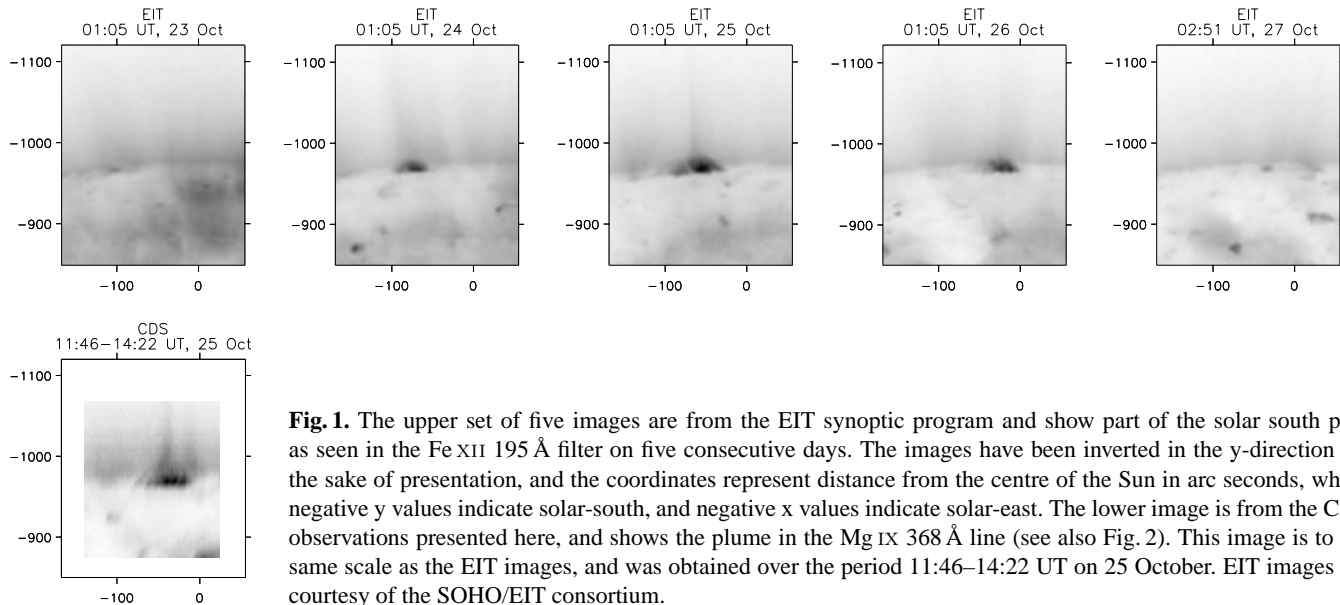


Fig. 1. The upper set of five images are from the EIT synoptic program and show part of the solar south pole as seen in the Fe XII 195 Å filter on five consecutive days. The images have been inverted in the y-direction for the sake of presentation, and the coordinates represent distance from the centre of the Sun in arc seconds, where negative y values indicate solar-south, and negative x values indicate solar-east. The lower image is from the CDS observations presented here, and shows the plume in the Mg IX 368 Å line (see also Fig. 2). This image is to the same scale as the EIT images, and was obtained over the period 11:46–14:22 UT on 25 October. EIT images are courtesy of the SOHO/EIT consortium.

Table 1. Properties of the FFNARR10/v8 study used in the present analysis.

Exposure time	100 s
Slit	2×240
Number of spectral windows	20
Window size	40 pixels
Raster x-size	10 pixels (20 arc sec)
Raster y-size	115 pixels (193 arc sec)
Duration	19 mins

513–633 Å, and are referred to as simply NIS1 and NIS2. Spectral resolutions are approximately 0.32 Å and 0.54 Å, respectively.

Telemetry constraints prevent the taking of complete NIS exposures for every observation. Instead, specific spectral windows are usually selected, with the choice of windows dependent on the particular solar feature to be studied; e.g., high temperature lines may be neglected in quiet Sun studies, whereas transition region lines may be neglected in off-limb studies.

A useful introduction to the spectroscopic capabilities of NIS is provided by Mason et al. (1997).

3.1. The CDS observing sequence

The CDS study used for the present polar plume observations is FFNARR10/v8, and the study parameters are given in Table 1. FFNARR10 was originally intended for the determination of filling factors in coronal loops, and so is focussed towards coronal density diagnostics such as Si X 356.0/347.4, Fe XII 338.3/364.5 and Fe XIV 353.8/334.2. There is excellent coverage of the $\log T \gtrsim 5.8$ temperature region, but only a few lines at temperatures below this, including He I 537.0 Å, O III 599.6 Å and O V 629.7 Å.

Due to the small width of the FFNARR10 rasters, the plume was observed by placing eight rasters side-by-side and so the total areal coverage is 160×193 arc sec². One scan of this area was made, taking 2 hours and 36 minutes. Images obtained with FFNARR10 are shown in Fig. 2 and are discussed further in Sect. 4.

3.2. Calibrating NIS spectra

The processes used in yielding calibrated NIS spectra are as follows. The FITS file containing the raw data is first *de-biased* to remove an electronic bias present in the data. All NIS data are contaminated with cosmic ray ‘hits’ (e.g., Fig. 1 and Sect. 3.1 of Harrison et al. 1997), and these were removed with the routine `cds_clean_spike` contained in the CDS software. The last step is performed using the routine `nis_calib` which converts the detected signal into units of $\text{erg cm}^{-2} \text{s}^{-1} \text{sr}^{-1}$.

The NIS calibration was revised on 23 December, 1998, and this new calibration is used in the present work.

3.3. Scattered light

A concern for any observation of regions above the solar limb is the contribution of scattered light to the observed line intensities. For the NIS/CDS observations presented here, scattering can occur within the instrument at two locations: (i) within the telescope section and, (ii) within the spectrograph section. Dealing with (ii) first, the scattering here arises from the spectrograph gratings. Thompson & Brekke (1999) suggest that the grating scattering is largely responsible for the near-uniform continuum seen in raw NIS spectra, and takes place only in the wavelength dispersion direction and not in the spatial direction. Evidence for this can be found in the fact that images of the NIS lines on the detector do not extend beyond the limits imposed by the slit size. Thus we neglect type (ii) scattering.

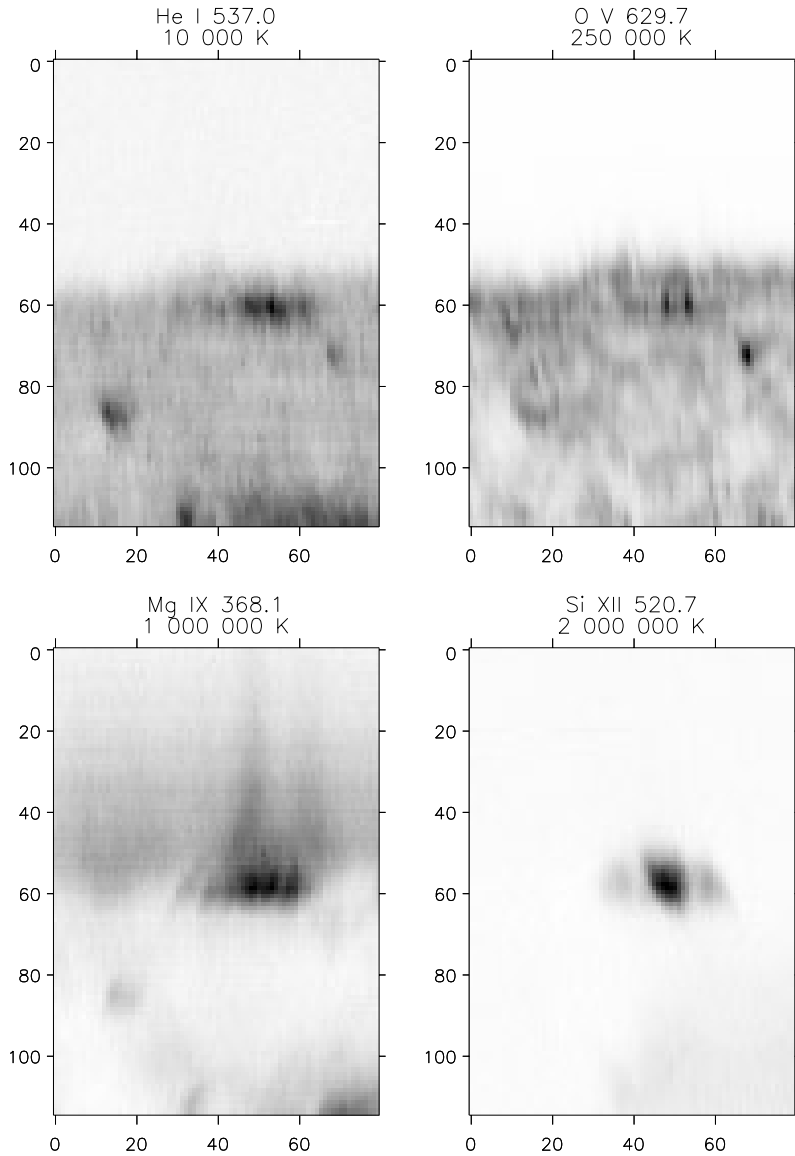


Fig. 2. Images of the plume in He I 584.3 Å, O V 629.7 Å, Mg IX 368.1 Å and Si XII 520.7 Å. For the sake of presentation, the images have been inverted in the y direction – the plume actually occurred at the south pole. The temperatures are the temperatures of maximum ionisation of the ions, while the axis scales are in CDS pixel numbers – see text for more details.

NIS shares the same telescope as the Grazing Incidence Spectrometer (GIS) of CDS, and the extent of telescope scattering has been discussed by David et al. (1997) in relation to the O VI 173 Å line observed by GIS. These authors have derived a routine to determine the contribution of scattered light to the intensity of three types of spectral line at any wavelength and for any height above the limb. The three types are (a) optically thick chromospheric, (b) transition region, and (c) coronal. In the analysis of the off-limb regions, the emission lines considered here are principally formed over the temperature range $5.7 \leq \log T \leq 6.2$, and so case (c) applies here. The maximum distance above the limb (and thus the location where scattering is most important) considered in the present work is ≈ 100 arc sec. David (private communication) has computed scattered light contributions of 10% at 300 Å and 5% at 500 Å at 100 arc sec above the limb for type (c) lines. These contributions will affect the emission measure analysis presented in Sects. 6.3 and 6.5, but as these values are upper limits and smaller than

the errors in the measured line intensities and errors introduced due to the emission measure method used, they will be ignored.

4. An overview of the observations

The plume analysed here was observed by CDS on the 25th of October, 1996, over the period 11:46–14:22 UT. EIT also observed the plume through its synoptic program and five images from consecutive days around the 25th are shown in Fig. 1. The lifetime of 2–3 days suggested by these images is typical of plumes. These EIT images (and also those of CDS) have been inverted in the y-direction for presentation purposes – the plume actually occurred at the solar south pole.

Images from the CDS observation of the plume in the He I 537.0 Å, O V 629.7 Å, Mg IX 368.1 Å, and Si XII 520.7 Å lines are shown in Fig. 2. The coordinate system used for these plots is based on CDS pixels: there are 8 rasters each of 10×115 pixels in size, and they are placed next to each other giving a total area of 80×115 pixels. In terms of dis-

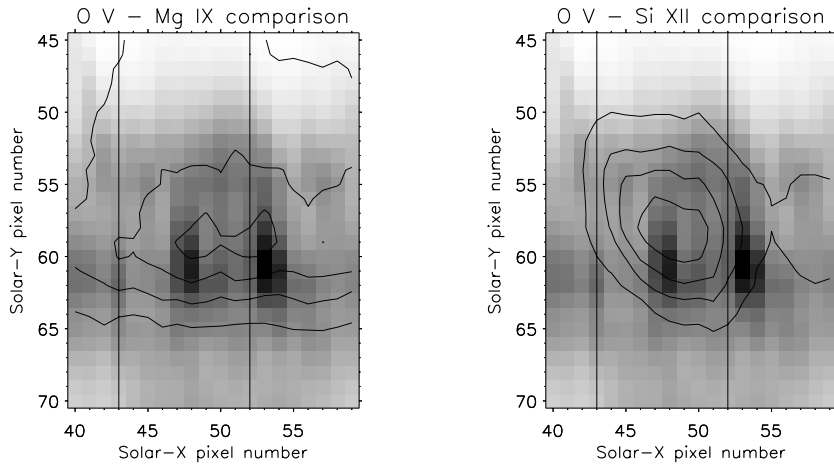


Fig. 3. A close-up of the plume base in the O V image of Fig. 2, with the Mg IX and Si XII images over-plotted as contours. The vertical lines indicate the region chosen for the plume analysis in Sect. 6; see also Fig. 8.

tances on the Sun, 1 x-pixel=2.03 arc sec=1470 km, and 1 y-pixel=1.68 arc sec=1218 km. In the rest of this paper, we will refer to pixel positions and Fig. 2 can be used for reference.

The Mg IX image shows that there are in fact two plumes side-by-side in the field-of-view, and this is more clearly seen in the ‘x-slices’ shown in Fig. 8. We will only analyse the data from the stronger of the two plumes

It is clear that, above the limb, the plume is only visible in the Mg IX line implying that the plasma principally has a temperature close to $\log T = 6.0$. Si XII is rarely seen in coronal holes and suggests that the plume base is not unlike a bright point or small active region. Complex structure can be seen at the plume base in the Mg IX image, indicating that the magnetic field is not a simple unipolar field, consistent with the MDI observations discussed in Sect. 2.1. The two strong brightenings seen in the O V line at the plume base coincide with the brightest of the Mg IX bright points, although the Mg IX brightenings are found 2 y-pixels higher up (Fig. 3).¹ The Si XII brightening is centred just above the left-hand brightening – see Fig. 3 – and lies directly under the plume (indicated by the vertical lines).

The magnetic topology suggested by the images is shown in Fig. 4. A small dipole, the footpoints of which can be seen in O V, lies under the unipolar field of the coronal hole. The fact that the Si XII emission lies directly above one of the footpoints suggests that this footpoint has opposite polarity to the surrounding field and so one may expect magnetic reconnection to occur above this footpoint, giving rise to high temperature plasma. When reconnection takes place, high pressure plasma from the dipole can escape along open field lines.

This situation is not unlike the X-ray jet model proposed by Shibata et al. (1994) and Yokoyama & Shibata (1995). It is rather surprising, however, that the plume temperature above the base is not hotter than observed.

Considering the off-limb part of the plume, some basic properties can be seen by looking at the stronger lines (a more de-

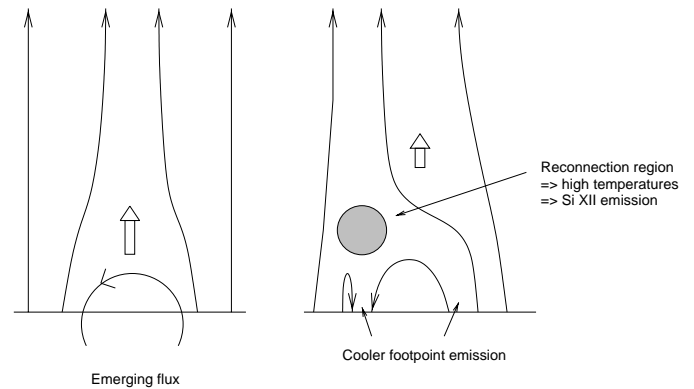


Fig. 4. A schematic interpretation of the plume emission. Arrowed lines represent magnetic field lines, while the large arrows denote the direction in which these lines move. If a bipolar region emerges beneath unipolar field, then the reconnection region would be expected to occur above one of the footpoints, consistent with observation.

tailed study is performed in Sect. 6). Fig 5 shows how the O V 629.7 Å and Mg IX 368.1 Å lines fall off above the limb in both the coronal hole background and the plume (the background has been subtracted from the plume). In the background the limb-brightening can be seen in both lines, while the maxima seen in the plume data mark the base of the plume. The Mg IX emission falls off gradually in both the background and plume, with the plume gradient being larger than that for the background. As expected, the O V line falls off very sharply with height, although there is still a significant signal at the largest heights that is likely due to scattered disk light.

A crude indication of the variation of temperature in the plume can be obtained by plotting ratios of the Ca x 557.8 Å, Mg IX 368.1 Å and Mg x 624.9 Å lines, which are formed at temperatures around 650 000 K, 950 000 K and 1 100 000 K, respectively. Fig. 6 shows the Mg x/Mg IX and Mg IX/Ca x ratios. The former clearly shows an increasing ratio with height in the background, whereas in the plume it is rather more constant. This indicates that the temperature in the background is rising with height, whereas in the plume it is constant. Although the plume appears to be hotter than the background (as the Mg x/Mg IX

¹ As discussed earlier, CDS takes exposures of the y spatial dimension and the spectral dimension simultaneously in all the lines, and so in comparing images in different lines, the x-axes are aligned exactly. The y-axis alignment has an accuracy of around a pixel.

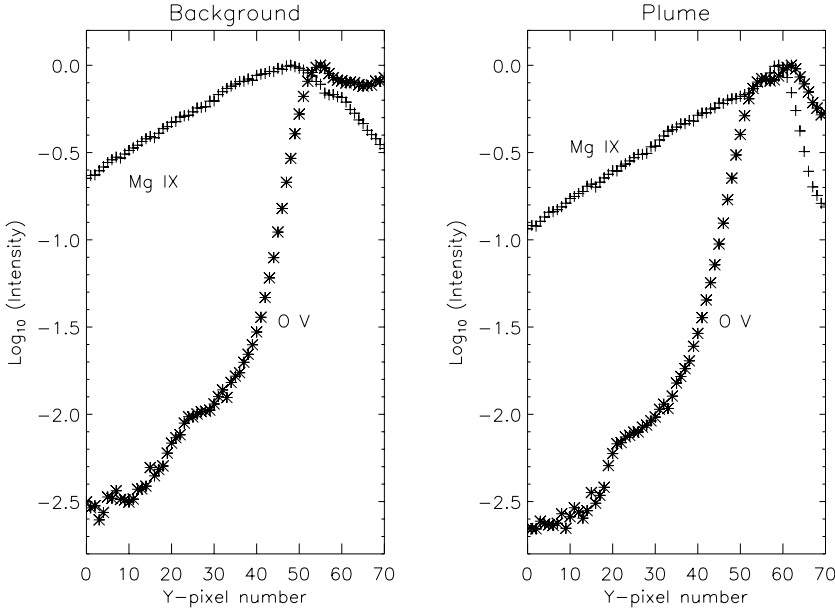


Fig. 5. Plots showing the fall off in the O V and Mg IX line intensities for the coronal hole background and plume. Pixel number zero is farthest from the limb. The background intensities have been subtracted from the plume intensities, and the intensities have been scaled so that the maxima are 1.

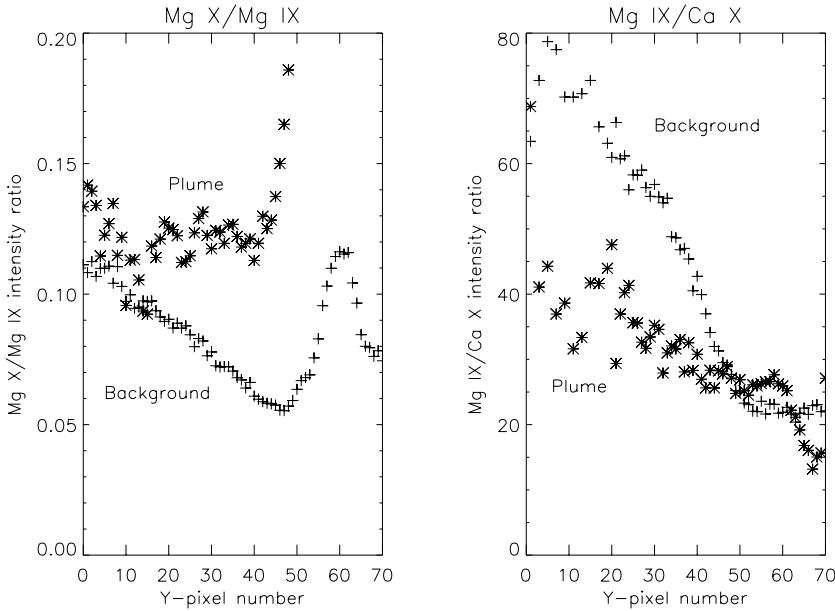


Fig. 6. Plots showing the variation of the Mg X/Mg IX and Mg IX/Ca X ratios with height for the coronal hole background and plume. Pixel number zero is farthest from the limb, and the background intensities have been subtracted from the plume intensities.

ratio is at least as large at all heights), in contradiction to the EIT data for other plumes discussed in Sect. 2.1, extrapolation of the data to greater heights would give larger temperatures in the background. The Mg IX/Ca X ratio also indicates increasing temperature with height in the background, and more uniform temperatures in the plume.

The fact that the Mg X/Mg IX ratio seems to level off at around y-pixel 43 suggests that the region above this height should be treated separately from that below. Thus, in Sect. 6, plasma properties of this region are studied.

5. Theory

Before proceeding to the detailed analysis of the plume, the notation used in the following sections will be introduced. Con-

sider a column of plasma with unit cross-sectional area. The intensity, I , of an emission line from this column is given by

$$4\pi I = 0.83 \Delta E Ab(X) \int n_j A_{ji} N_e F(T) dh \quad (1)$$

where 0.83 is the ratio of protons to free electrons (a constant for $T > 10^5$ K), ΔE is the energy of the photon released by the $j \rightarrow i$ transition, $Ab(X)$ is the abundance of the emitting element X relative to hydrogen, n_j is the fractional population of the emitting level j , A_{ji} is the radiative decay rate for the $j \rightarrow i$ transition, N_e is the electron number density, and $F(T)$ is the ionisation fraction of the emitting ion. Defining

$$\mathcal{G}(T, N_e) = 0.83 \Delta E Ab(X) \frac{n_j A_{ji}}{N_e} F(T) \quad (2)$$

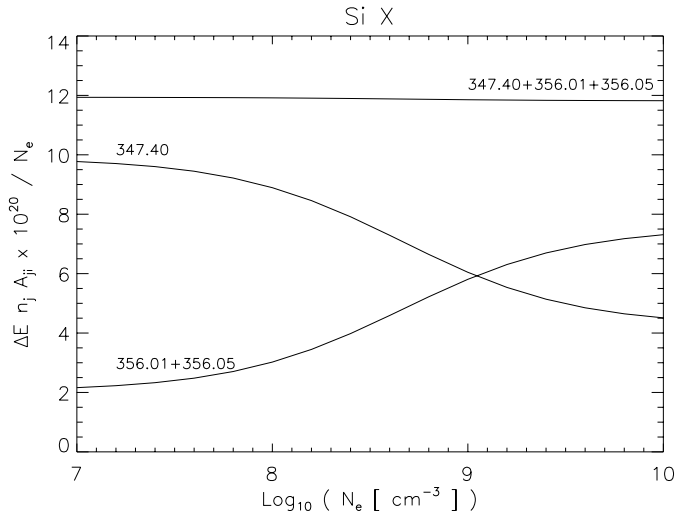


Fig. 7. Variation of the quantity $\Delta E n_j A_{ji} / N_e$ with N_e for the Si X lines observed by CDS at 347.4 Å and 356.0 Å (this latter is a blend of two lines). For neither line does the $n_j \propto N_e$ relation hold, but summing the lines gives this relation.

and

$$\phi(T)dT = N_e^2 dh, \quad (3)$$

we have

$$4\pi I = \int \mathcal{G}(T, N_e) \phi(T) dT \quad (4)$$

where $\phi(T)$ is the *differential emission measure* (d.e.m.).

The definition of \mathcal{G} is chosen because, typically, $n_j \propto N_e$, and so \mathcal{G} is weakly dependent on N_e . By choosing to analyse only lines for which $n_j \propto N_e$, we essentially eliminate the problem of determining N_e from the problem of determining $\phi(T)$. This restriction, however, rules out many lines seen by NIS but one solution is to sum two or more lines from an ion such that the different N_e dependencies cancel out. The example of Si X is shown in Fig. 7.

In trying to determine ϕ , there are two methods usually employed. The first is originally due to Pottasch (1963) and later modified by Jordan & Wilson (1971), in that \mathcal{G} is assumed to be constant over some narrow temperature interval, and zero outside of this interval. \mathcal{G} can then be taken outside of the integral, and the remaining integral is termed the *emission measure* (or, more strictly, the *column emission measure* in the example above), which can be determined directly from the atomic parameters and the observed intensity. An alternative is to treat the determination of ϕ as an *inversion problem*, and the form of ϕ can be deduced via an iterative procedure from a set of observed intensities (e.g., Withbroe 1975, Craig & Brown 1976).

The atomic data required for the A_{ji} and the computation of the n_j were obtained from version 2 of the CHIANTI database (Dere et al. 1997, Landi et al. 1999), except where indicated. The data required for the ion fractions, $F(T)$, are from Arnaud & Rothenflug (1985) and Arnaud & Raymond (1992).

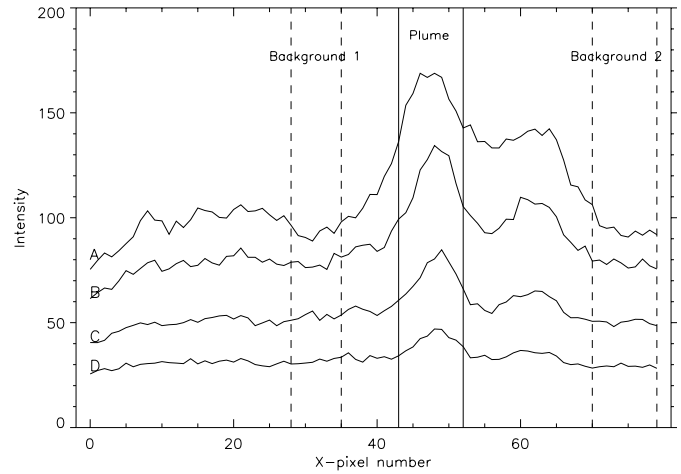


Fig. 8. Variation of the Mg IX 368.1 Å intensity across the plume. The vertical lines indicate the regions chosen to define the plume and the background. The four profiles are from the four regions A, B, C and D which are defined in Sect. 6.1.

6. Above the limb

As discussed above, the fall-off in the Mg IX and Mg X lines above the limb suggests that the region between pixels 0 and 43 should be treated distinctly from the plume base. As many of the lines to be studied are weak, substantial summing over spatial areas is required and this is described below.

6.1. Region specification

The region between y-pixels 0 and 43 is divided into four based on the fall-off of the Mg IX line in the coronal hole background: the regions being chosen so that approximately equal numbers of counts in the line are present in each region. We thus define region A to be pixels 38 to 43; region B, pixels 31 to 37; region C, pixels 20 to 30; and region D, pixels 0 to 19. In Fig. 8, the variation of the Mg IX line in the solar-x direction is shown with summations performed over these four regions. The vertical lines in this plot define the solar-x regions that are used as the coronal hole background and plume in the following analysis. Thus, in considering a line intensity from, e.g., region C in the plume, the line intensity has been averaged over a total of $10 \times 11 = 110$ spatial pixels.

Table 2 gives the intensities for each of the emission lines used in the present study in the four regions of the coronal hole background and plume. The intensities were derived by performing non-linear least squares fits of the spectra to Gaussians with a linear background, while error bars take account of both fitting errors, photon statistics and detector noise (see Thompson 1997).

6.2. Densities

As will be shown in the following section, the plasma above the solar limb is predominantly around $\log T = 6.0$ and so to determine the density we require density diagnostics for which

Table 2. Line intensities in $\text{erg cm}^{-2} \text{s}^{-1} \text{sr}^{-1}$ in the coronal hole background and polar plume. The background intensities have been subtracted from the plume intensities.

	Ion	Line	Region			
			A	B	C	D
Coronal hole background	Mg X	624.9	21.3 ± 1.1	21.2 ± 1.1	18.2 ± 1.0	12.9 ± 0.7
	Mg IX	368.1	331 ± 17	285 ± 14	205 ± 10	122 ± 6
	Mg VIII	339.0	27.3 ± 2.1	18.5 ± 1.7	10.4 ± 1.2	4.8 ± 0.8
	Mg VII	367.7	32.2 ± 2.9	19.8 ± 1.8	11.5 ± 1.4	6.4 ± 1.0
	Si X	347.4	18.2 ± 1.6	17.3 ± 1.5	14.9 ± 1.3	11.5 ± 0.9
	Si X	356.0	9.7 ± 1.3	9.0 ± 1.5	7.8 ± 0.9	5.9 ± 0.7
	Si IX	345.1	38.9 ± 2.8	33.7 ± 1.9	24.9 ± 1.5	16.1 ± 1.2
	Si IX	349.9	30.5 ± 2.0	24.5 ± 1.6	16.4 ± 1.3	9.2 ± 0.7
	Si VIII	319.8	79.8 ± 3.8	60.2 ± 2.8	36.9 ± 1.9	17.6 ± 1.3
	Fe XII	364.5	9.0 ± 1.7	8.1 ± 1.6	7.3 ± 1.1	5.6 ± 0.7
	Fe XI	352.1	18.9 ± 1.9	17.0 ± 1.5	14.3 ± 1.2	9.9 ± 1.0
	Fe X	345.7	27.3 ± 1.9	22.2 ± 1.7	15.7 ± 1.3	8.6 ± 1.0
	Ca X	557.8	12.1 ± 0.8	8.1 ± 0.6	5.0 ± 0.5	2.6 ± 0.2
Plume	Mg X	624.9	24.1 ± 2.2	17.8 ± 2.1	11.0 ± 1.4	5.7 ± 1.1
	Mg IX	368.1	188 ± 28	142 ± 23	88.8 ± 15.2	47.0 ± 8.3
	Mg VIII	339.0	12.1 ± 3.7	10.0 ± 2.5	5.6 ± 1.9	3.7 ± 1.3
	Mg VII	367.7	18.1 ± 4.7	12.7 ± 3.0	7.6 ± 2.4	2.7 ± 1.9
	Si X	347.4	19.5 ± 3.1	13.3 ± 2.5	7.5 ± 2.1	3.9 ± 1.6
	Si X	356.0	17.7 ± 2.5	11.0 ± 2.3	7.6 ± 1.7	2.8 ± 1.6
	Si IX	345.1	29.2 ± 4.8	22.6 ± 3.8	12.4 ± 2.7	6.7 ± 1.9
	Si IX	349.9	30.6 ± 3.7	22.8 ± 3.2	13.5 ± 2.5	6.7 ± 1.4
	Si VIII	319.8	46.1 ± 7.8	31.9 ± 6.4	19.8 ± 3.7	8.3 ± 1.8
	Fe XII	364.5	16.0 ± 3.0	8.3 ± 2.7	4.0 ± 1.9	1.5 ± 1.1
	Fe XI	352.1	18.0 ± 3.8	13.8 ± 2.7	7.7 ± 1.9	3.8 ± 1.5
	Fe X	345.7	16.7 ± 3.5	12.4 ± 2.9	7.5 ± 2.1	3.7 ± 1.5
	Ca X	557.8	9.4 ± 1.4	6.5 ± 1.0	3.6 ± 0.7	1.6 ± 0.3

the ion has a maximum abundance close to this temperature. Table II of Mason et al. (1997) suggests Si IX 345.13/341.95, 349.87/345.13, Si X 356.03/347.40, and Fe XII 338.26/364.47 are the most useful. The Si IX 341.95 Å line is not observed with the FFNARR10 study, while the Fe XII 338.26 Å line is very weak, and so we are left with Si IX 349.87/345.13 and Si X 356.03/347.40. Fig. 9 shows the NIS region C background spectrum in the 344–358 Å wavelength range, where the Si IX and Si X density diagnostic lines are clearly seen.

At low densities, transitions induced by the photospheric radiation field can have a significant effect on the level balance of ions, and this is certainly the case for both Si IX and Si X. We account for these extra processes in the ion level balance through the method outlined by Flower & Pineau des Forêts (1973; Sect. 3). In order to compute the *dilution factor* (see Eq. 11 of Flower & Pineau des Forêts) we need to know how far above the solar surface lies the emitting plasma. For the coronal hole background, this was done by estimating where the solar limb occurred in the raster through the limb brightening curve of O V (Fig. 5) and comparing it with the data presented on page 59 of Mariska (1992). The solar-y pixel position of the limb was thus found to be 58, and by taking average pixel positions for the four regions, the distance above the limb of the regions was estimated and converted to dilution factors of 0.377, 0.359, 0.337 and 0.309, for regions A, B, C and D, respectively.

For the plume, the position of the plume base is required and this was determined from the variation of both the O V and Mg IX lines with height (Fig. 5) to be at solar-y pixel 67. Comparing this with the position of the limb and assuming that the plume is perpendicular to the solar surface gives a plume inclination of 10° . Including projection effects, the dilution factors for the four regions are then 0.352, 0.337, 0.317 and 0.292.

The ratios and derived densities are given in Table 3 – the error bars for the plume data are rather large owing to the fact that the background intensities have been subtracted.

There were some difficulties found in fitting the Si X lines, particularly 356.0 Å, due to weak lines either side of the fitted line (e.g., Fig. 9). In these cases, nearby areas free from lines were chosen as the spectral background.

For the coronal hole background, the Si IX data show a clear trend of falling density with height. The Si X data do not show the same fall-off but are consistent with the Si IX data on account of the larger error bars. The Si X ratio values lie rather close to the low density limit and a possible cause for the near-identical densities found in each region is that the current theoretical low density limit may be in error – the present work suggesting the limit should be slightly higher (at around 0.52).

Doschek et al. (1997) have utilised the Si VIII 1440.49/1445.76 ratio to estimate densities in a coronal hole observed by the SUMER instrument on board SOHO.

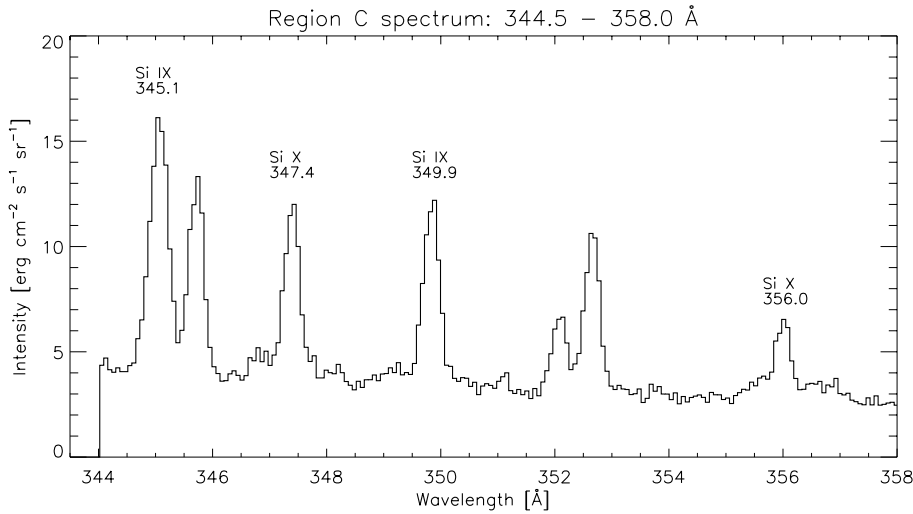


Fig. 9. An NIS spectrum from region C of the coronal hole background, illustrating the strength of the Si IX and Si X density diagnostic line pairs. Note that the continuum on which the lines sit mainly consists of light from outside of the NIS wavebands scattered by the grating.

Table 3. Electron number densities (in units of cm^{-3}) derived from the Si IX and Si X diagnostics in the four off-limb regions of the plume and background. The subscript ‘lo’ indicates that the observed ratio lies below the low density limit of the diagnostic. The densities have been evaluated assuming the temperatures \bar{T} given in Table 5.

Region	Quantity	Region			
		A	B	C	D
Background	Si IX 349.9/345.1	0.785 ± 0.076	0.726 ± 0.063	0.660 ± 0.067	0.572 ± 0.062
	Log N_e	$8.21^{+0.13}_{-0.13}$	$8.12^{+0.11}_{-0.12}$	$8.01^{+0.13}_{-0.14}$	$7.86^{+0.13}_{-0.15}$
	Si X 356.0/347.4	0.534 ± 0.087	0.521 ± 0.097	0.521 ± 0.078	0.516 ± 0.071
	Log N_e	$8.15^{+0.21}_{-0.37}$	$8.13^{+0.24}_{-0.45}$	$8.16^{+0.19}_{-0.31}$	$8.19^{+0.17}_{-0.26}$
Plume	Si IX 349.9/345.1	1.048 ± 0.213	1.008 ± 0.219	1.088 ± 0.313	1.007 ± 0.350
	Log N_e	$8.65^{+0.40}_{-0.34}$	$8.59^{+0.39}_{-0.35}$	$8.73^{+0.78}_{-0.50}$	$8.60^{+0.72}_{-0.56}$
	Si X 356.0/347.4	0.905 ± 0.193	0.830 ± 0.234	1.015 ± 0.364	0.712 ± 0.492
	Log N_e	$8.84^{+0.24}_{-0.28}$	$8.74^{+0.30}_{-0.39}$	$8.98^{+0.47}_{-0.51}$	$8.58^{+0.63}_{-1.0}$

For the region 25–97 arc sec above the limb that is considered in the present work, Doschek et al. find the density falls from around $\log N_e = 7.9$ to 7.3, i.e., the rate at which the density is falling is a factor of 2 greater than that found here. Wilhelm et al. (1998) have performed a similar analysis for sets of plume and interplume observations, and find a less steep density fall-off from $\log N_e = 7.9$ to 7.5 over the same heights in the interplume region.

As expected, Table 3 shows the plume densities derived here to be higher than in the background regions. The Si IX data do not suggest that the density is falling off with height although the error bars are rather large. The density enhancement over the background is between 2.5 and 5.5. The Si X data suggest higher densities than Si IX although, within the error bars on the data, there is agreement. The plume densities found by Wilhelm et al. (1998) from SUMER data are very similar to the interplume densities at low heights, but gradually become greater with height. At 100 arc sec above the limb, the plume density is $\log N_e = 7.6$, only around 25% greater than in the interplume region. This confirms that the plume studied in the present work is particularly intense.

6.3. Relative ion emission measures

In this section emission measure distributions are derived for both the background coronal hole and the plume in the off-limb regions. Two methods for doing this were mentioned in Sect. 5, but neither are appropriate for the conditions above the limb because of the narrow temperature distribution. The method used here is described below.

6.3.1. Method

Firstly, Sect. 5 suggested lines should be used in the emission measure analysis for which $n_j \sim N_e$ and, if necessary, use sums of lines. Table 4 shows the lines used here. When referring to the lines in this table, we will tend to refer to simply the ion, e.g., ‘Si IX’ will refer to the blend of the four Si IX lines.

In determining the emission measure, we consider a discretised d.e.m. curve defined such that $\phi_i = \phi(T_i)$ where the T_i are distributed at intervals of $\Delta \log T = 0.05$. Taking $\mathcal{G}_i = \mathcal{G}(T_i)$, the ϕ_i distribution required to reproduce an observed line intensity must satisfy

$$4\pi I = \sum_i \mathcal{G}_i \phi_i \Delta T_i \quad (5)$$

Table 4. The emission lines used in the derivation of the plasma distribution. In the density insensitive column, \times indicates that $n_j A_{ji}/N_e$ varies with density; \circ that the line varies weakly with density; and \checkmark that the line is insensitive to density. For both the \times and \circ lines densities of 10^8 and $10^{8.55}$ were used for the background and plume, respectively, in the emission measure analysis. T_{mem} is the temperature of maximum emission of the ion line, i.e., the temperature at which the \mathcal{G} function (Eq. 2) has its maximum value. The two values of T_{mem} given for the iron ions are from the Arnaud & Rothenflug (1985) and Arnaud & Raymond (1992) ion balance calculations, respectively.

Ion	Observed wavelengths	CHIANTI wavelengths	NIS bandpass	T_{mem}	Density insensitive?
Si VIII	319.8	319.83	1	5.90	\times
Si IX	[345.1,349.9]	344.95, 345.12, 349.79, 349.87	1	6.04	\circ
Si X	[347.4,356.0]	347.40, 356.01, 356.05	1	6.14	\checkmark
Mg VII	367.7	367.67, 367.68	1	5.80	\circ
Mg VIII	339.0	339.01	1	5.92	\checkmark
Mg IX	368.1	368.07	1	5.98	\circ
Mg X	624.9	624.94	2	6.04	\checkmark
Fe X	345.7	345.72	1	5.98/6.04	\circ
Fe XI	352.7	352.66	1	6.06/6.10	\times
Fe XII	364.5	364.47	1	6.14/6.16	\times
Ca X	557.8	557.77	2	5.82	\checkmark

Table 5. Plasma distributions deduced from the silicon ion line ratios and expressed as percentages for the coronal hole background and plume. Also given are values of \bar{T} , weighted average temperatures, deduced from the plasma distributions.

	Region	q_i values				$\text{Log } \bar{T}$
		$\text{Log } T_i = 5.95$	6.00	6.05	6.10	
Background	A	6%	94%			6.00
	B		86%	14%		6.01
	C		55%	45%		6.02
	D		10%	90%		6.05
Plume	A		41%	48%	11%	6.04
	B		43%	57%		6.03
	C		43%	57%		6.03
	D		36%	64%		6.03

or, writing $Q_i = \phi_i \Delta T_i$,

$$4\pi I = \sum_i \mathcal{G}_i Q_i \quad (6)$$

(Note that $\sum_i Q_i \sim N_e^2 h$, where h is the emitting column height.)

It is possible to take all of the observed intensities from the ions of Table 4 and attempt to find a Q_i distribution that will reproduce the observed values. However, this masks uncertainties in the atomic data for the ions and the assumed abundances of the ions.

The method used here is to first consider ions from a single element (silicon in the case here) to derive a Q_i distribution, and then use this to see how well it reproduces the observed intensities from the other elements

The silicon ions are chosen because the T_{max} 's of the ions span the temperature range $5.9 \leq \log T \leq 6.1$ (unlike the iron ions), and all three ions yield relatively strong, clean lines (unlike the magnesium ions where the Mg VIII 339.0 Å line is

weak in CDS spectra, and the Mg VII line is partially blended with the Mg IX 368.1 Å line).

Rather than deriving absolute Q_i values, we first consider only *ratios* of observed lines to derive $q_i = Q_i / \sum_i Q_i$ values. For silicon this means we search for a q_i distribution that reproduces the observed Si VIII/Si IX and Si X/Si IX ratios. This is done by *manually* adjusting the q_i values until the best fit to the observed ratios is found. The scope for such a choice is small on account of the particular shapes of the \mathcal{G} functions for the three silicon ions (Fig. 10), which show that the peak of the Si IX function lies below those of Si VIII and Si X. From Table 2 one can see, however, that the intensities of the summed 345.1 and 349.9 Å Si IX lines are greater than those of the Si VIII and Si X lines in most of the regions, thus requiring non-zero Q_i values only at $\log T_i = 6.00$ and 6.05 .

The q_i values, expressed as percentages, are given in Table 5. The silicon ratios predicted (R_{pred}) can be compared with the observed ratios (R_{ob}), and the values are given in Table 6. As the R_{ob} have been used to derive the R_{pred} , the $R_{\text{pred}}/R_{\text{ob}}$ are all close to one.

Taking the q_i distributions and applying them to the magnesium ions, one can predict values for the Mg VII/Mg IX, Mg VIII/Mg IX and Mg X/Mg IX ratios. The $R_{\text{pred}}/R_{\text{ob}}$ values are given in Table 6. Values close to one (implying agreement with the silicon q_i distribution) are only found for Mg VIII. For Mg VII, R_{ob} lies above the predicted value by around a factor 2, while for Mg X R_{ob} lies below the predicted values by a factor 2–3. These discrepancies will be returned to in the following section.

For the iron ions, the Fe XI/Fe X and Fe XII/Fe X ratios were considered for both the Arnaud & Rothenflug (1985) and Arnaud & Raymond (1992) ion balance data. The $R_{\text{pred}}/R_{\text{ob}}$ values in Table 6 clearly show that better agreement with the silicon ion is found with the Arnaud & Rothenflug (1985) data.

On account of the narrow temperature distributions, it is useful to evaluate a weighted temperature average,

Table 6. This table gives a comparison between line ratios predicted from the silicon q_i distribution and the actual observed ratios. For each element a reference ion is chosen – Si IX, Mg IX and Fe X – and the numbers in the table are the ratio of the predicted ratio to the observed ratio. As the silicon ions were used to give the q_i distribution, the silicon ratios are all close to 1. For iron there are two sets of entries that are derived using the Arnaud & Rothenflug (1985; A&Roth) and Arnaud & Raymond (1992; A&Ray) ion balance calculations. The error bars are purely from the errors in the measured line intensities given in Table 2.

	Element	Line	Region			
			A	B	C	D
Background	Silicon	Si VIII 319.8	1.10 ± 0.08	1.13 ± 0.07	1.14 ± 0.08	1.15 ± 0.11
		Si X [347,356]	1.11 ± 0.10	1.13 ± 0.10	1.14 ± 0.10	1.15 ± 0.10
	Magnesium	Mg VII 367.7	0.56 ± 0.06	0.68 ± 0.07	0.69 ± 0.09	0.46 ± 0.08
		Mg VIII 339.0	0.94 ± 0.09	1.09 ± 0.12	1.26 ± 0.15	1.26 ± 0.23
		Mg X 624.9	2.83 ± 0.22	2.70 ± 0.18	2.64 ± 0.21	2.88 ± 0.22
	Iron	Fe XI 352.7	1.23 ± 0.15	1.22 ± 0.14	1.18 ± 0.14	1.11 ± 0.17
		(A&Roth) Fe XII 364.5	0.86 ± 0.17	0.99 ± 0.21	1.09 ± 0.19	1.09 ± 0.19
	Iron	Fe XI 352.7	1.65 ± 0.20	1.62 ± 0.19	1.58 ± 0.19	1.54 ± 0.24
		(A&Ray) Fe XII 364.5	1.91 ± 0.38	2.12 ± 0.45	2.29 ± 0.39	2.42 ± 0.41
Plume	Silicon	Si VIII 319.8	1.00 ± 0.20	1.13 ± 0.26	1.04 ± 0.24	1.26 ± 0.35
		Si X [347,356]	1.00 ± 0.14	1.14 ± 0.20	1.04 ± 0.24	1.26 ± 0.48
	Magnesium	Mg VII 367.7	0.38 ± 0.11	0.42 ± 0.12	0.43 ± 0.16	0.60 ± 0.44
		Mg VIII 339.0	0.95 ± 0.33	0.89 ± 0.27	0.98 ± 0.38	0.76 ± 0.30
		Mg X 624.9	2.12 ± 0.36	2.09 ± 0.42	2.11 ± 0.44	2.25 ± 0.59
	Iron	Fe XI 352.7	1.04 ± 0.31	0.95 ± 0.34	1.03 ± 0.39	1.06 ± 0.60
		(A&Roth) Fe XII 364.5	0.67 ± 0.19	0.80 ± 0.32	1.01 ± 0.56	1.40 ± 1.18
	Iron	Fe XI 352.7	1.37 ± 0.41	1.28 ± 0.46	1.38 ± 0.52	1.43 ± 0.81
		(A&Ray) Fe XII 364.5	1.34 ± 0.38	1.70 ± 0.68	2.13 ± 1.18	2.98 ± 2.50

$$\bar{T} = \frac{\sum_i Q_i T_i}{\sum_i Q_i} \quad (7)$$

and this is also given in Table 5. The \bar{T} values clearly show a trend of increasing temperature in the interplume region, but near constant temperature in the plume.

The densities used in this analysis are $\log N_e = 8.00$ for the coronal hole background, and $\log N_e = 8.55$. *The densities from Table 3 are not used.* This is because we are determining relative emission measure distributions, where specification of the precise density is not important.

6.4. Comparing different elements

A next step is to compare different elements and this is done by taking the ions formed closest in temperature to Si IX: Mg IX, Fe X and Ca X (the only calcium ion). Again, the ratio of the theoretical ratios to the observed ratios are computed using the silicon q_i distributions and the results are presented in Table 7. For iron, only the Arnaud & Rothenflug (1985) ion balance calculations were used. Photospheric element abundances (Anders & Grevesse 1989, Grevesse et al. 1992) are assumed in these comparisons. Each of the elements has a low first ionisation potential, and so the element fractionation often observed in the solar corona and discussed by, e.g., Feldman (1992), is not important here.

The Mg IX/Si IX values in Table 7 are all less than one. Interestingly, the values in the background fall with height. This is because, although, the observed Mg IX/Si IX ratio remains fairly constant with height, the rising temperature found from

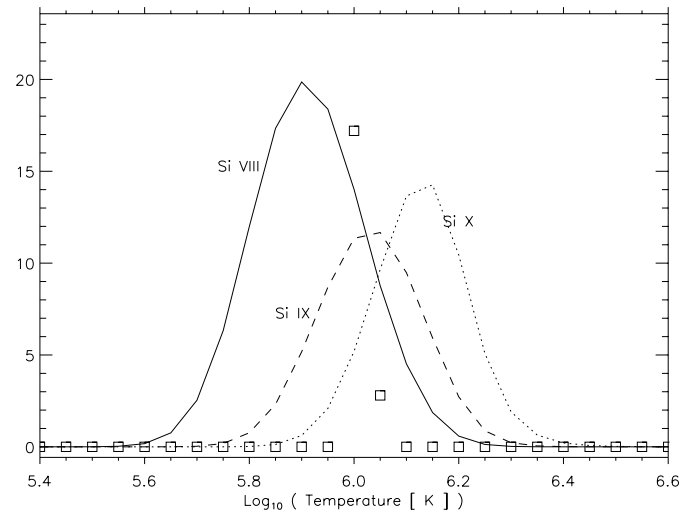


Fig. 10. Plot illustrating how the Q_i distribution is chosen. The three curves show the Q_i functions for the Si VIII, Si IX and Si X lines, while the boxes give the Q_i values that fit the observed silicon ratios from region B of the coronal hole background (see Table 5).

the silicon q_i distribution (Table 5, last column) coupled with the differences in the T_{\max} for Mg IX and Si IX (Table 4), mean that the Mg IX/Si IX ratio is predicted to fall with height. Thus better agreement between predictions and observations could be achieved through the Mg IX ion fraction curve moving to higher temperatures to overlap better with Si IX. This would have knock-on effects for Mg X and Mg VII which would also

Table 7. Comparisons of theory with observation for ions of different elements, assuming photospheric abundances apply. Values different from 1 indicate either abundance variations or problems with the atomic physics.

	Line	Region			
		A	B	C	D
Background	Mg IX 368.1	0.70 ± 0.05	0.64 ± 0.04	0.56 ± 0.04	0.47 ± 0.04
	Fe X 345.7	0.64 ± 0.06	0.66 ± 0.06	0.67 ± 0.06	0.76 ± 0.10
	Ca X 557.8	0.16 ± 0.01	0.18 ± 0.02	0.19 ± 0.02	0.18 ± 0.02
Plume	Mg IX 368.1	0.70 ± 0.13	0.73 ± 0.14	0.67 ± 0.15	0.63 ± 0.16
	Fe X 345.7	0.82 ± 0.19	0.84 ± 0.22	0.79 ± 0.25	0.83 ± 0.37
	Ca X 557.8	0.12 ± 0.02	0.14 ± 0.03	0.14 ± 0.03	0.16 ± 0.04

Table 8. Values of the absolute emission measure, α , and column depth, h , for the coronal hole background and plume. Also given for the plume is the derived plume diameter, d . Entries of the form $a(+b)$ represent the number $a \times 10^{+b}$.

	Quantity	Region			
		A	B	C	D
Background	α (cm ⁻⁵)	7.79(+26)	6.42(+26)	4.52(+26)	2.73(+26)
	h (cm)	2.96(+10)	3.69(+10)	4.31(+10)	5.21(+10)
Plume	α (cm ⁻⁵)	6.04(+26)	4.49(+26)	2.56(+26)	1.32(+26)
	d (cm)	3.85(+9)	3.78(+9)	1.13(+9)	1.06(+9)

move to higher temperatures, helping to resolve the discrepancies noted for these ions in the previous section.

For Fe X, the observed ratio lies above the predicted ratio in all regions by around 20–30%. This could be due to some small Si/Fe abundance anomaly, but is as likely to be due to inaccuracies in the atomic data.

There are major problems for calcium, where the theoretical ratio is consistently lower than the observed ratio *by factors of 5–8*. Although Ca X is formed at a lower temperature than Si IX, such a large discrepancy was not seen for Mg VII (which has considerable temperature overlap with Ca X). It is suggested here that the problem lies in the ionisation fraction for Ca X: the Arnaud & Rothenflug calculations give a maximum ionisation fraction of only 8% for this ion on account of the neighbouring Ca XI ion having a very large ion fraction. Thus small changes in the ionisation or recombination rates are likely to have a large effect on the Ca X ion fraction. The observed data presented here suggest the Ca X ionisation fraction should be larger than presently predicted by Arnaud & Rothenflug.²

6.5. Absolute emission measure

The absolute intensities measured in both the plume and the background can be used to yield indirect estimates of the depth of the emitting region as follows. From Eq. 6,

$$4\pi I = \sum \mathcal{G}_i Q_i = \alpha \sum \mathcal{G}_i q_i \quad (8)$$

where the q_i are the fractions given in Table 5. α can be written as $N_e^2 h$, where h is the column depth of the emitting region.

² Note also that Ca X belongs, along with Fe XVI, to the sodium iso-electronic sequence. Arnaud & Raymond (1992) found large differences for the ion fraction of Fe XVI compared to the Arnaud & Rothenflug (1985) values, with the new fraction being considerably larger.

For the plume, however, we note that the values of I stem from averages over the width of the plume. By assuming a cylindrical geometry for the plume, $h = \frac{\pi}{4}d$, where d is the diameter of the plume.

The values of α are given in Table 8 and were derived from Eq. 8 using the observed Si IX intensities from Table 2, \mathcal{G} values from CHIANTI (and assuming a photospheric silicon abundance, Anders & Grevesse 1989), and q_i values from Table 5. The values of h , for the background, and d , for the plume, were derived from the α values using the Si IX densities from Table 3.

To compare the h and d values with other dimensions, it is to be noted that $R_\odot = 6.96 \times 10^{10}$ cm, while the width of the plume is taken to be $d_{\text{ob}} \sim 10$ X-pixels $\approx 1.4 \times 10^9$ cm (Fig. 8). The coronal hole background values are as expected, bearing in mind that the entire coronal hole ($\sim 1 R_\odot$ in size) will contribute to the line emission, and that the column depth would be expected to increase with height as the coronal hole expands.

There appears to be a discrepancy between the derived plume diameters and d_{ob} for regions A and B, with the former being too large by almost a factor 3. However, considering that a factor 3 can be achieved by varying the value of $\log N_e$ by 0.24, and the error bars quoted in Table 3 are larger than this value, it is felt that the values of d in Table 8 are in reasonable agreement with d_{ob} . Thus, there is no need to consider filling factors less than one, or non-photospheric abundances.

7. The plume base

7.1. Temperature

As readily seen from Fig. 2 the plume base contains plasma at a large range of temperature. If we are to assume that the high temperature region seen in Si XII in the base plays an integral part in the plume's properties, then an upper limit on the tem-

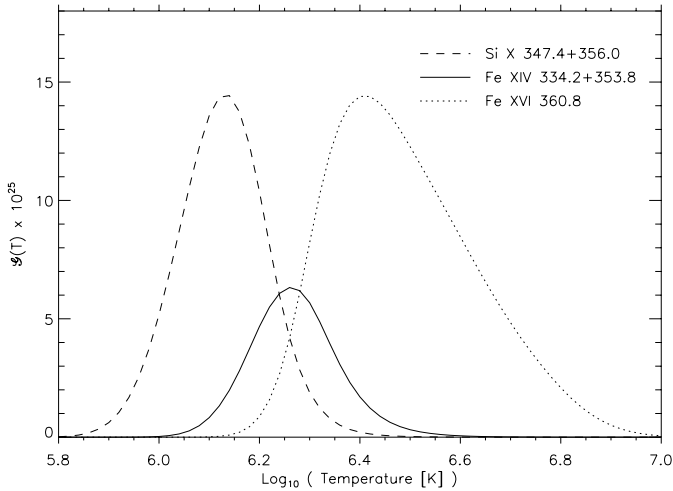


Fig. 11. A comparison of the $\mathcal{G}(T)$ functions for lines of Si X, Fe XIV and Fe XVI.

perature of this region is useful. To obtain this upper limit the Si X 347.4, 356.0 Å, Fe XIV 334.2, 353.8 Å, and Fe XVI 360.8 Å lines can be used. For the density sensitive line pairs, summing the lines gives a density insensitive ‘line’. In Fig. 11 the \mathcal{G} functions for these lines are plotted and the most striking feature is that the Fe XIV function is considerably smaller than those for Si X and Fe XVI and so, with virtually any plasma distribution, at least one of Si X or Fe XVI will be stronger than Fe XIV. However, considering the spectra from the brightest three pixels in the Fe XIV image of the plume base (see Fig. 12 and Table 9) the combined Fe XIV intensity is $739 \text{ erg cm}^{-2} \text{ s}^{-1} \text{ sr}^{-1}$, whereas the Si X and Fe XVI values are $629 \text{ erg cm}^{-2} \text{ s}^{-1} \text{ sr}^{-1}$ and $402 \text{ erg cm}^{-2} \text{ s}^{-1} \text{ sr}^{-1}$. Inspection of Fig. 11 shows that theory makes such values impossible unless there are errors in the atomic physics or element abundances.

Question marks over the CHIANTI atomic data for Fe XIV have been raised by Young et al. (1998; Sect. 13.6), while Young & Mason (1998; Sect. 3.2) report new Fe XIV calculations performed by P.J. Storey (see also Storey et al. 1999) that show significant differences with those contained in the CHIANTI database. In particular, the sum of the $\Delta E n_j A_{ji} / N_e$ factors for the blend of the 334.2 and 353.8 Å lines predicted by CHIANTI is $9.73 \times 10^{-20} \text{ erg cm}^3 \text{ s}^{-1}$, whereas with the new calculations it is 1.66×10^{-19} – a factor of 1.71 higher.³ This raises the Fe XIV curve in Fig. 11 by this factor, in far better agreement with the observed intensities. Returning to the question of the maximum temperature at the plume base, the low value of the Fe XVI intensity implies $\log T \leq 6.3$.

7.2. Densities

The strong brightening seen in Si XII at the base of the plume (Figs. 2 and 3) is also seen in the density sensitive Fe XIV 334.2, 353.8 Å line pair – see Fig. 12. The over-plotted contours on

³ These quantities are largely insensitive to the temperature and density, but the values $\log T = 6.26$ and $\log N_e = 9.0$ were used here.

this image divide it according to the intensity of the 334.2 Å line, and the intensities are given explicitly in Table 9. This table also gives the average 334.2 and 353.8 intensities in each region and the derived densities, and it can be seen that, although the intensities fall off by almost a factor of 3, the densities actually increase slightly although, within the error bars on the data, a constant density is also consistent.

The Fe XIV emitting region is approximately circular in projection (Fig. 12) and so, by assuming that it is a spherical volume, we can compare the *depth* of the emitting region as deduced from atomic physics parameters to the actual observed *width*, in a similar fashion to Sect. 6.5.

Suppose that the brightening has a uniform density and temperature. Then, considering the line intensity from the centre of the brightenings, Eq. 1 gives

$$4\pi I = 0.83 \Delta E Ab(X) n_j A_{ji} F(T) N_e d_{\text{em}}, \quad (9)$$

where d_{em} is the brightening diameter deduced from emission line intensities. Here we consider the sum of the two Fe XIV lines at 334.2 Å and 353.8 Å, and so

$$4\pi(I_{334} + I_{353}) = 0.83(\Delta E_{334} n_6 A_{334} + \Delta E_{353} n_7 A_{353}) \times Ab(\text{Fe}) N_e F(T) d_{\text{em}}. \quad (10)$$

(The numbers 6 and 7 refer to the levels of the CHIANTI Fe XIV model which give rise to the 334.2 and 353.8 lines, respectively.) From Table 9, we take the average intensity from the centre three pixels of the brightening as $I_{334} + I_{353} = 739 \text{ erg cm}^{-2} \text{ s}^{-1} \text{ sr}^{-1}$, and the density as $\log N_e = 9.48$. The temperature is assumed to be the temperature of maximum abundance (T_{max}) of Fe XIV, i.e., 6.26 from Arnaud & Raymond (1992), giving $F(T) = 0.242$. With the new Fe XIV atomic data described in the previous section, we have $\Delta E_{334} n_6 A_{334} + \Delta E_{353} n_7 A_{353} = 4.92 \times 10^{-10} \text{ erg s}^{-1}$. For the abundance of iron we use the photospheric value of Grevesse et al. (1992), i.e., $Ab(\text{Fe}) = 3.24 \times 10^{-5}$. We thus find $d_{\text{em}} = 9.60 \times 10^8 \text{ cm}$, while the observed width of the brightening is $d_{\text{ob}} \approx 14 \text{ x-pixels} \approx 1.96 \times 10^9 \text{ cm}$ from Fig. 12. Thus if the assumption of a photospheric iron abundance is correct, the filling factor of the brightening is 0.5.

Performing a density analysis for the Si X lines (Table 10) also shows that the electron density is marginally lower in the very brightest pixels. The Si X densities are lower than those found for Fe XIV but, as Si X is formed at lower temperatures than Fe XIV (Fig. 11), this is likely due to the Si X lines originating from a different (lower density) volume of plasma.

8. The Mg/Ne abundance

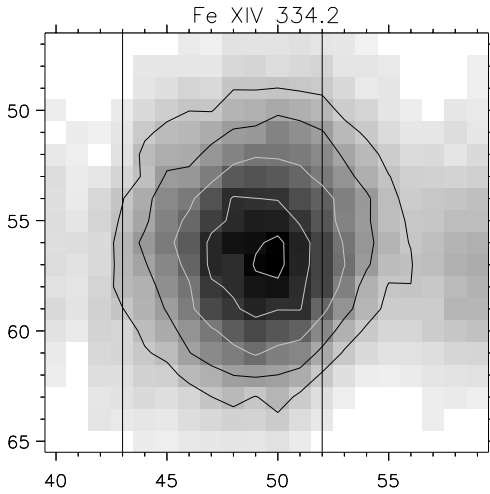
The finding by Widing & Feldman (1992) that the Mg/Ne abundance is enhanced by an order of magnitude in a polar plume compared to the photosphere was a key result and has been cited as evidence that plumes contribute little to the high speed solar wind (e.g., Sect. 3 of Wang 1994). Given that Mg/Ne abundance ratio measurements are possible with CDS (e.g., Young & Mason 1997), it is reasonable to ask what is found in the present case.

Table 9. Electron densities derived for the regions indicated in Fig. 12. The regions are chosen on the basis of the intensity of the 334.2 Å line. Intensities are in units of $\text{erg cm}^{-2} \text{s}^{-1} \text{sr}^{-1}$.

Region	No. of pixels	Intensity		Ratio	Density
		334.2 Å	353.8 Å		
$I_{334} > 497$	3	512 ± 23	227 ± 20	0.443 ± 0.044	$9.48^{+0.09}_{-0.09}$
$497 \geq I_{334} > 417$	19	444 ± 21	219 ± 17	0.493 ± 0.045	$9.58^{+0.07}_{-0.09}$
$417 \geq I_{334} > 289$	27	350 ± 20	173 ± 16	0.494 ± 0.054	$9.58^{+0.09}_{-0.10}$
$289 \geq I_{334} > 193$	44	239 ± 17	124 ± 12	0.519 ± 0.062	$9.62^{+0.10}_{-0.11}$
$193 \geq I_{334} > 119$	45	153 ± 13	78.9 ± 10.4	0.516 ± 0.081	$9.62^{+0.13}_{-0.16}$

Table 10. Si x electron densities derived for regions within the plume base, based on the intensity of the 347.4 Å line. Intensities are in units of $\text{erg cm}^{-2} \text{s}^{-1} \text{sr}^{-1}$.

Region	No. of pixels	Intensity		Ratio	Density
		347.4 Å	356.0 Å		
$I_{347} > 343$	3	358 ± 20	392 ± 21	1.095 ± 0.085	$9.15^{+0.10}_{-0.10}$
$343 \geq I_{347} > 289$	17	316 ± 18	372 ± 19	1.177 ± 0.090	$9.24^{+0.11}_{-0.10}$
$289 \geq I_{347} > 231$	37	258 ± 17	311 ± 18	1.205 ± 0.106	$9.28^{+0.13}_{-0.13}$
$231 \geq I_{347} > 181$	47	206 ± 16	234 ± 16	1.136 ± 0.118	$9.20^{+0.14}_{-0.14}$
$181 \geq I_{347} > 134$	54	158 ± 14	168 ± 15	1.063 ± 0.134	$9.11^{+0.16}_{-0.14}$

**Fig. 12.** Image of the plume base in Fe XIV 334.2 Å. The contours indicate the areas used in the density analysis – see Table 9. The vertical lines denote the region defined in Sect. 4 as the plume.

A difficulty lies with the fact that, of the neon lines lying in the NIS wavebands, only the Ne VI 558.6 Å line profile is clearly seen with the FFNARR30 study, and even then it is partially blended with a Ne VII line. A separate Ne VII line at 559.9 Å is observed at the very edge of the Ne VI window (Fig. 14). When considering the off-limb spectra, further problems are encountered because the Ne VI 558.6 Å line lies in the wing of the much stronger Ca x 557.8 Å line. These combine to prevent an estimate of the Mg/Ne relative abundance being made in the off-limb section. (Note that Widing & Feldman 1992 had available the strongest line in the Ne VII spectrum at 465.2 Å with which to do analysis.)

At the base of the plume progress can be made. The two small brightenings seen in the O V line (Fig. 2) are also seen in the Ne VI 558.6 Å and Mg VI 349.2 Å lines. By summing spectra from the two brightenings, we derive the intensities for the Mg VI 349.2 Å, Mg VII 367.7 Å, Ne VI 558.6 Å and Ne VII 559.9 Å lines given in Table 11. The Ne VII line intensity was derived by comparing the FFNARR10 spectral window with data from a NISAT_S study, which takes complete NIS spectra (Fig. 14). Such a comparison shows that approximately one half of the Ne VII profile is found in the FFNARR10 window, and so an estimate of the Ne VII intensity can be made from the amplitude of the observed feature and the instrumental width of NIS2 lines (around 0.54 Å). With the 559.9 intensity, it was possible to then estimate the contribution of Ne VII to the line at 558.6 Å as the Ne VII 558.6/559.9 ratio is insensitive to the plasma conditions with a value of 1.24.

With these line intensities, the Mg/Ne abundance ratio can then be estimated via the following method. Writing

$$4\pi I = \bar{\mathcal{G}}(N_e) EM(h) \quad (11)$$

where $EM(h)$ is the *column emission measure*, and $\bar{\mathcal{G}}$ is a constant such that

$$\mathcal{G}(N_e, T) = \begin{cases} \bar{\mathcal{G}}(N_e) & |\log T - \log T_{\text{mem}}| < 0.15 \\ 0 & |\log T - \log T_{\text{mem}}| > 0.15 \end{cases} \quad (12)$$

and

$$\bar{\mathcal{G}}(N_e) = \frac{\int \mathcal{G}(N_e, T) dT}{T_{\text{mem}}(10^{0.15} - 10^{-0.15})}, \quad (13)$$

we can evaluate $EM(h)$ values for each of the ions. (With the above definition, $EM(h)$ is the average emission measure over the temperature interval $|\log T - \log T_{\text{mem}}| < 0.15$.)

For the evaluation of $\bar{\mathcal{G}}(N_e)$, CHIANTI v.2 data was used, together with an assumed density of 10^9 cm^{-3} and *photospheric*

Table 11. Line intensities and derived emission measures for the magnesium and neon lines. Also given are the atomic quantities, \bar{G} , and the temperatures of maximum emission, T_{mem} .

Line	Intensity	\bar{G}	$EM(h)$	T_{mem}
Mg VI 349.2	51.3 ± 7.0	1.49(-24)	26.64	5.64
Mg VII 367.7	98.0 ± 16.9	1.05(-24)	27.07	5.80
Ne VI 558.6	51.3 ± 3.2	2.42(-24)	26.43	5.64
Ne VII 559.9	5.0 ± 1.1	1.24(-25)	26.70	5.72

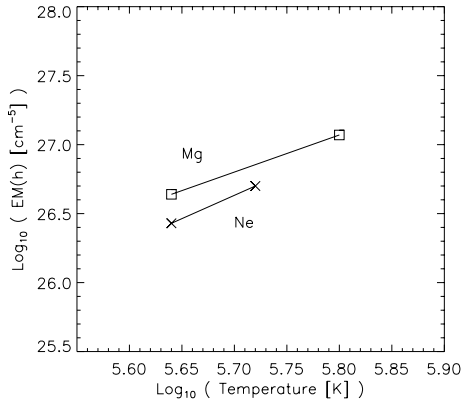


Fig. 13. A plot showing the derived emission measures of Table 11.

abundances ($Ab(\text{Mg}) = 3.80 \times 10^{-5}$, Anders & Grevesse 1989, $Ab(\text{Ne}) = 1.20 \times 10^{-4}$, Grevesse et al. 1992). The derived values of $EM(h)$ are given in Table 11 and displayed graphically in Fig. 13.

Forcing the magnesium and neon emission measure distributions to agree with each other would require the Mg/Ne relative abundance to be increased by a factor $10^{0.183} = 1.52$ over the photospheric value, implying only a very small FIP-effect.

9. Conclusions

In this paper we have presented a detailed analysis of EUV spectra from a CDS/SOHO observation of an intense polar plume seen on the 25th of October 1996. The key findings in relation to the physical properties of the plume are as follows:

- The base of the plume has a complex structure: two strong brightenings are seen in O V which are seen up to temperatures of one million degrees (Mg IX). The base temperature has a maximum of two million degrees, at which temperature only a single large brightening is seen. The Fe XIV 353.8/334.2 density diagnostic was used to give densities of $2.5 \times 10^9 \leq N_e \leq 5.6 \times 10^9 \text{ cm}^{-3}$ for this brightening. In addition to the main brightenings (which lie directly under the main body of the plume), there can be seen four other weaker brightenings that appear related to the plume (see the Mg IX image of Fig. 2).
- Above the limb, the plume has a narrow (~ 0.15 dex) temperature distribution which peaks at $1\,000\,000 \leq T \leq 1\,100\,000 \text{ K}$. There was no indication of changing temperature with height. Density diagnostics of Si IX and Si X

were used to derive electron number densities of $3.8\text{--}9.5 \times 10^8 \text{ cm}^{-3}$. A trend for changing density with height was not found.

- A section of coronal hole background close to the plume was analysed using the same techniques, and was found to have a narrower temperature distribution and increasing temperature with height. The Si IX density diagnostic showed density decreasing with height, whereas the Si X diagnostic showed constant density. The Si X densities may indicate that the ratio was at the low density limit.
- By studying absolute intensities, estimates of the column depth of the emitting plasma could be made for both the above-limb section of the plume and the hot brightening at the base. Above the limb, the data was consistent with a filling factor of 1, whereas for the brightening a filling factor of 0.5 was found.
- The Mg/Ne relative abundance at the two strong transition region brightenings seen at the base of the plume was derived, and found to be a factor of only 1.5 higher than the photospheric value. Thus there is no evidence of a strong Mg/Ne enhancement such as found by Widing & Feldman (1992).

The plume presented here was particularly intense and, as such, allowed a clear separation from the coronal hole background above the limb which is not always possible for more ‘normal’ plumes. The basic appearance of the plume in the different emission lines (Fig. 2) clearly shows that some form of heating is taking place at the plume base, as required by, e.g., the model of Wang (1994). This model shows the temperature rising sharply, falling, then rising more gradually again over the first $0.2 R_{\odot}$ (Fig. 1 of Wang 1994). The sharp rise and fall off are found here and relate to the intense 2 million K brightening seen at the plume base. Above this brightening the temperature becomes uniform (e.g., the Mg X/Mg IX plot of Fig. 6) out to the limit of the observations ($0.1 R_{\odot}$).

The images of the plume base suggest the emergence of a small dipole may be the cause of the plume (Figs. 3 and 4), but such a scenario would imply non-steady heating, whereas Wang’s model implicitly assumes steady heating.

The densities and temperatures in the off-limb section of the plume are consistent with a constant pressure, whereas a simple hydrostatic model would require a falling pressure. This can be resolved by including a velocity gradient in the model (e.g., Ahmad & Withbroe 1977), and in the present case an accelerating plasma would be required through the plume. No estimate is made here of the magnitude of this acceleration as the noise in the plume density estimates are large (Table 3).

In addition to the above, we report the following additional results that relate to the NIS calibration and atomic physics:

- From the emission measure analysis performed on both the coronal hole background and plume in the off-limb regions, we found the Ca X 557.8 Å observed intensity to be considerably stronger than predicted by factors of 5–8. It would seem that the Arnaud & Rothenflug (1985) ion balance calculations may be in error for Ca X, and we suggest that the Ca X ion fraction should be larger than currently predicted.

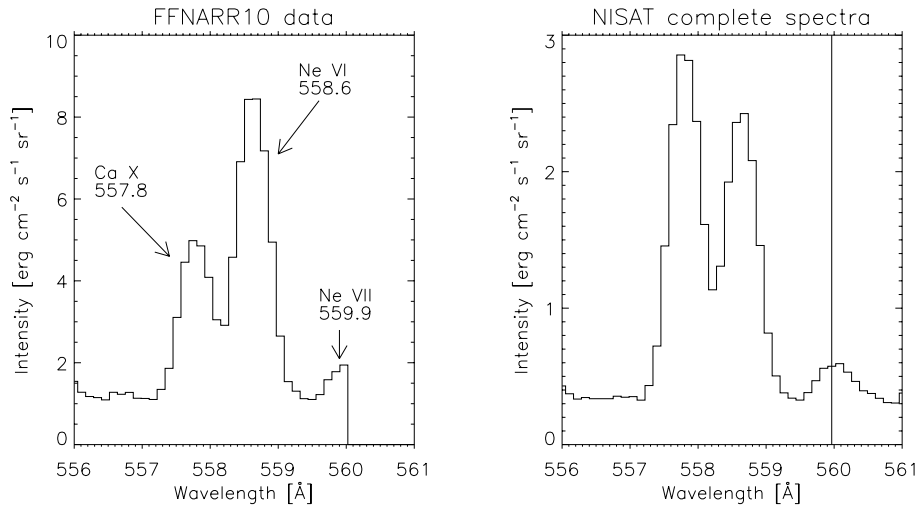


Fig. 14. A comparison of spectra from the FFNARR10 and NISAT_S studies in the region 556–561 Å. The NISAT_S study takes complete NIS spectra and so the entire line profile of the Ne VII 559.9 line can be seen. The vertical line in the right-hand plot denotes the right-most pixel in the FFNARR10 window.

- The Arnaud & Rothenflug (1985) and Arnaud & Raymond (1992) ion balance calculations were compared for the Fe X–XII ions in the emission measure analysis performed on the plume and coronal hole background. The results clearly suggest that the Arnaud & Rothenflug (1985) calculations agree better with observation. Note that an analysis of NIS data by Young & Mason (1998) for Fe XIV and Fe XVI showed the *opposite* result.
- Again from the emission measure analysis performed on the off-limb portions of the plume and coronal hole background, comparisons of the magnesium and silicon line intensities suggested that the magnesium ion fraction curves should be shifted to higher temperatures by around 0.05 dex, relative to the silicon curves.

Acknowledgements. PRY and HEM acknowledge the support of PPARC. SOHO is a project of international collaboration between ESA and NASA. JAK was supported by NASA grant W-19,191.

References

- Ahmad I.A., Withbroe G.L., 1977, *Sol. Phys.* 53, 397
- Anders E., Grevesse N., 1989, *Geochim. Cosmochim.* 53, 197
- Arnaud M., Raymond J.C., 1992, *ApJ* 398, 394
- Arnaud M., Rothenflug R., 1985, *A&AS* 60, 425
- Craig I.J.D., Brown J.C., 1976, *A&A* 49, 239
- David C., Gabriel A.H., Bely-Dubau F., 1997, Measurement of Above-limb Coronal Intensities. In: Proc. of the Fifth SOHO Workshop, ESA SP-404, 313
- David C., Gabriel A.H., Bely-Dubau F., et al., 1998, *A&A* 336, L90
- DeForest C.E., Hoeksema J.T., Gurman J.B., et al., 1997, *Sol. Phys.* 175, 393
- Del Zanna L., Hood A.W., Longbottom A.W., 1997, *A&A* 318, 963
- Dere K.P., Landi E., Mason H.E., Monsignori-Fossi B.M., Young P.R., 1997, *A&AS* 125, 149
- Doschek G.A., Warren H.P., Laming J.M., et al., 1997, *ApJ* 482, L109
- Feldman U., 1992, *Phys. Scripta* 46, 202
- Fisher R., Guhathakurta M., 1995, *ApJ* 447, L139
- Flower D.R., Pineau des Fôrets G., 1973, *A&A* 24, 181
- Grevesse N., Noels A., Sauval A.J., 1992, Photospheric Abundances. In: Proc. of the First SOHO Workshop, ESA SP-348, 305
- Harrison R.A., Sawyer E.C., Carter M.K., et al., 1995, *Sol. Phys.* 162, 233
- Harrison R.A., Fludra A., Pike C.D., et al., 1997, *Sol. Phys.* 170, 123
- Hassler D.M., Wilhelm K., Lemaire P., Schühle U., 1997, *Sol. Phys.* 175, 375
- van de Hulst H.C., 1950, *Bull. Astron. Soc. Neth.* 11, 150
- Jordan C., Wilson R., 1971, In: Macris C.J. (ed.) *Physics of the Solar Corona*. Reidel, Dordrecht, 199
- Landi E., Landini M., Dere K.P., Young P.R., Mason H.E., 1999, *A&AS* 135, 339
- Mariska J.T., 1992, *The Solar Transition Region*. Cambridge University Press, Cambridge
- Mason H.E., Monsignori-Fossi B.F., 1994, *A&AR* 6, 123
- Mason H.E., Young P.R., Pike C.D., et al., 1997, *Sol. Phys.* 170, 143
- Pottasch S.R., 1963, *ApJ* 137, 945
- Shibata K., Nitta N., Strong K.T., et al., 1994, *ApJ* 431, L51
- Storey P.J., Mason H.E., Young P.R., 1999, *A&A*, submitted
- Thompson W.T., 1997, CDS Software Note, no. 49, ver. 3
- Thompson W.T., Brekke P., 1999, *Sol. Phys.*, in preparation
- Wang Y.-M., 1994, *ApJ* 435, L153
- Wang Y.-M., Sheeley Jr. N.R., 1995, *ApJ* 452, 457
- Widing K.G., Feldman U., 1992, *ApJ* 392, 715
- Wilhelm K., Marsch E., Dwivedi B.N., et al., 1998, *ApJ* 500, 1023
- Wilhelm K., Bodmer R., 1998, *Space Sci. Rev.* 85, 371
- Withbroe G.L., 1975, *Sol. Phys.* 45, 301
- Yokoyama T., Shibata K., 1995, *Nat* 375, 42
- Young P.R., Mason H.E., 1997, *Sol. Phys.* 175, 523
- Young P.R., Mason H.E., 1998, *Space Sci. Rev.* 85, 315
- Young P.R., Landi E., Thomas R.J., 1998, *A&A* 329, 291